# Construction of Graphitic Carbon Nitride-based Photocatalyst with Strong Built-in Electric Field via π-π Stacking Interaction Boosting Photocatalytic $CO_2$ Reduction

Yanrui Li*[a], Linda Wang [a], Xiang Gao [a], Yingying Xue [a], Bozhan Li [a], Xiaolin Zhu*[b]

# Table of contents

## Experimental Procedures

### Preparation of catalyst

**Synthesis of crystalline nitride carbon (NCN).** All reagents were used without further purification. graphitic carbon nitride (GCN) was synthesized following published procedures [1]. In brief, starting from melamine (10 g) calcined in a lidded quartz boat at 550 °C in argon for 4h with a ramping rate of 5 °C min$^{-1}$, yellow bulk GCN powder (yield 4~5 g) was synthesized after cooling to room temperature, which was thoroughly ground into a powder for further processing and analysis. High crystalline nitride carbon (NCN) was prepared from GCN with a molten-salt (KSCN) method as reported previously [2]. Thoroughly mixing GCN (3.0 g) with KSCN (6.0g, dried overnight at 140 °C in vacuum), the mixture was transferred into an alumina boat in a tube furnace, which was heated at 140 °C for 8 h under argon, then at 400 °C for 1 h, and at 500 °C for 30 min. Following that, a yellow solid was suspended in water and washed with deionized water and ethanol several times to remove residual potassium ions and dried at 60 °C in a vacuum oven.

**Synthesis of TPHAP.** Sodium 2,5,8-tri-(4'-pyridyl)-1,3,4,6,7,9-hexaazaphenalenate, TPHAP was synthesized following the published paper [3]. 4-pyridylamidine hydrochloride (9.10 g, 57.7 mmol) was thoroughly mixed with sodium tricyanomethanide ($NaC(CN)_3$, 1.32 g, 11.6 mmol) and transferred into a Teflon-lined stainless autoclave heating at 200 ºC for 16 h. Following that, a brown bulk was obtained and thoroughly ground into power, which was then dispersed into 2M HCl aqueous solution to obtain a pellucid aqueous layer and acid-insoluble substance. The acid-insoluble substance was then filtered and moved, leaving the pellucid brown aqueous. Subsequently, the brown aqueous was neutralized with a 5M NaOH aqueous solution and new sediment solid was formed. Collecting and washing the sediment solid with water and ethanol.

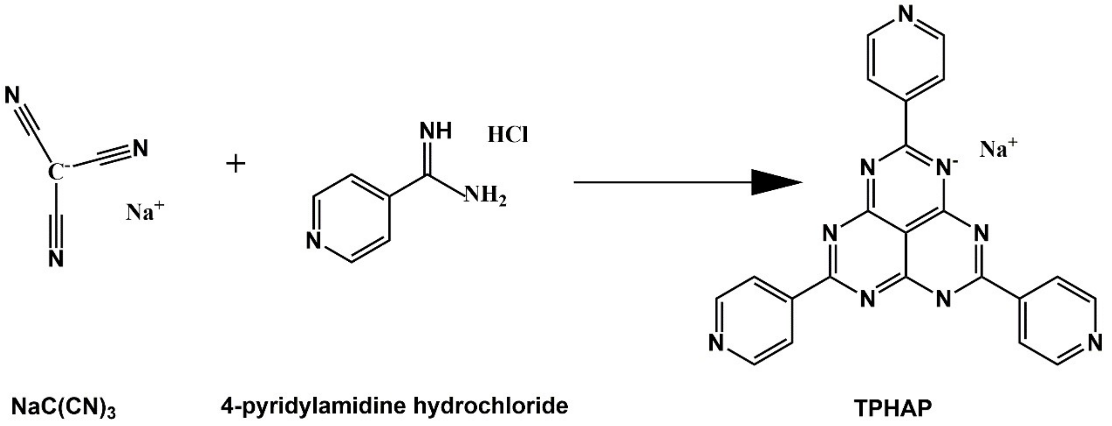

**Scheme S1**. The reaction scheme for the synthesis of TPHAP.

**Synthesis of TPNCN*m*.** 100 mg of NCN was dispersed into 20 mL of deionized water with ultrasonication for 60 min. Meanwhile, different amounts of TPHAP (1mg, 5mg, 10mg) were dispersed in 5 mL of ethanol under ultrasonication for 20 min and then slowly injected into the NCN aqueous solution. Additionally, these mixtures were extensively washed with deionized water and ethanol several times, and then dried at 60 °C under vacuum overnight. The obtained yellow solid was transferred into an alumina boat in a tube furnace at 100°C for 1 h under argon.

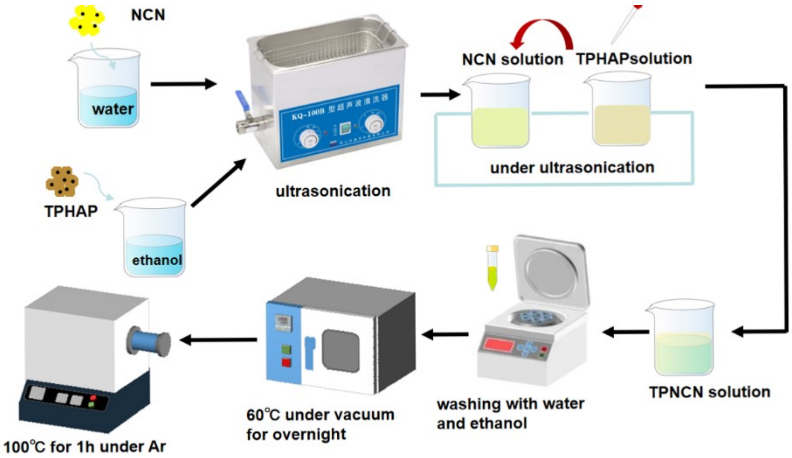

**Scheme S2**. Schemed fabrication process of TPNCN*m*

**Characterization.**

A MiniFlex 600 (Rigaku, Japan) with Cu-Kα radiation from ($\lambda$ = 1.5406 Å) was carried out to measure powder X-ray diffraction (XRD) patterns. A Bruker Tensor II spectrometer was utilized to obtain Fourier transform infrared (FTIR) spectra in the range of 4000-400 $cm^{-1}$. KRATOS Ultra DLD instrument equipped with a Al Ka source was performed to collect X-ray photoelectron spectroscopy (XPS) measurements. Shimadzu PE lambda 750 spectrophotometer equipped with an integrating sphere was utilized to achieve UV-Vis diffuse reflectance spectra (DRS). Atomic force microscopy (AFM) experiments were performed on an Asylum Research Cypher VRS (Oxford instruments) atomic force microscope equipped with a Scan Asyst-HR fast scanning module and a Kelvin probe. Shimadzu (UV3600) spectrometer was carried out to obtain the photoluminescence spectra (PL) excited by incident light of 315 nm and fluorescence lifetime spectrophotometer (Edinburgh, FLS1000) was utilized to obtain the time-resolved photoluminescence (TRPL) spectra excited by incident light of 350 nm. In-situ attenuated total reflectance (ATR)-FTIR spectra were performed on a diffuse reflectance infrared Fourier transform spectrometer (Bruker TENSOR II). The catalysts were loaded in the sample cell, following with bubbling into $CO_2$ flow with water vapor for 30 min. Through a quartz window of the sample cell, the light irradiation was shed on the sample.

Ultraviolet photoelectron spectroscopy (UPS) detection: UPS (Thermo Scientific, Escalab Xi+) measurements were carried out to detected the work function ($\Phi$) of samples with a He I UV source (hv = 21.22 eV). The work function was calculated according to the Equation (1) [4]:

$$\Phi = hv - E_{cutoff} \qquad (1)$$

Where the $E_{cutoff}$ refered to high-binding energy secondary electron cutoff. The valence band ($E_{VB}$) position was calculated as Equantion (2):

$$E_{VB} = hv - (E_{cutoff} - E_{femi}) \qquad (2)$$

Where the $E_{femi}$ referred to the energy different between the feimi level and valence band maximum.

Calculating the lifetime of photoexcited carrier: the time-resolved photoluminescence (TRPL) spectra were well fitted by the multi-exponential equation (3) and the average lifetime ($\tau_{avg}$) could be calculated by the equation (4) [5].

$$I_t = I_0 + A_1 \exp\left(\frac{t}{\tau_1}\right) + A_2 exp(\frac{t}{\tau_2}) \qquad (3)$$

$$\tau_{avg} = \frac{A_1\tau_1^2 + A_2\tau_2^2}{A_1\tau_1 + A_2\tau_2} \qquad (4)$$

where the $I_0$, τ, and A referred the baseline correction value, lifetime and pre-exponential factors.

**Electrochemical characterization**

All electrochemical measurements were carried out on an electrochemical analyzer (CHI660E, ChenHua, China) with a conventional three-electrode system in 0.2 M $Na_2SO_4$ solution. In the three-electrodes system, Pt electrode was used as the counter electrode, the Ag/AgCl electrode was the reference electrode, and working electrode was prepared by catalyst-coated ITO conductive glass. The Mott-Schottky (MS) analysis was recorded with the frequency of 500, 1000 and 1500 Hz. Electrochemical impedance spectroscopy (EIS) plots were detected with the frequency sweep range 100-106 Hz and the amplitude 5 mV. The incident light source utilized for photocurrent measurement was Xe lamp (PLS-SEX300D, PerfectLight, Beijing).

**Photocatalytic $CO_2$ reduction activity measurement.**

The $CO_2$ photoreduction performances measurement was evaluated in a 100 mL reactor. A glass bracket (2 cm in diameter), equipped with quartz sand chip (2 cm in diameter) supporting for dispersing catalyst, was put into this reactor before reaction to isolate water and sample. Before reaction, deionized water (2 ml) was added to the bottom of reactor and as-prepared catalysts (5 mg) was uniformly dispersed on the quartz sand chip, following with injecting mixture of $CO_2$ and $H_2O$ vapor for 30 min. The incident light sourcewas Xenon lamp (PLS-SEX300D, PerfectLight, Beijing) equipped with a UV-cut filter (λ > 400 nm). The photocatalytic reaction products in reactor were detected every 1 h with a gas chromatograph (GC, Huifen, GC 7820) with a flame-ionization detector (FID) and thermal conductivity detector(TCD). Apparent quantum yield (AQY) for CO production was calculated according to equation:

$$\text{AQY of CO (\%)} = \frac{2\times number\ of\ CO\ molecles}{number\ of\ incident\ photons} \times 100\%$$

**Computational Methods**

The density functional theory (DFT) calculations were performed with the generalized gradient approximation (GGA) and PBE functional [6]. The cutoff energy was set to be 435 eV for NCN and 517 eV for TPHAP, with Monkhorst-Pack *k*-point sets of 1 × 2 × 1 for NCN and 1 × 1 × 1 for TPHAP. The energy tolerance and force tolerance were considered as $2 \times 10^{-5}$ eV/atom and 0.05 eV/Å, respectively. The adsorption energies (Ea) of the adsorbates in $CO_2$ reduction were calculated as following:

$Ea = E_R^* - (ER + E^*)$ (5)

Where $E_R^*$ was the total energy of an adsorbate (R) adsorbed on the surface (*) and ER and E* are the energies of the single adsorbate and clean surface, respectively [7].

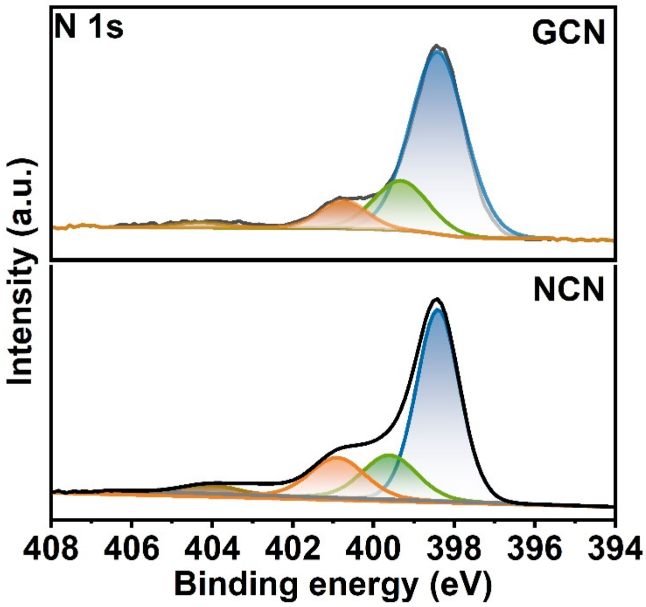

**Figure S1.** N 1s X-ray photoelectron spectroscopy (XPS) spectra of GCN and NCN.

The phenomenon that partial replacement of amino groups by cayanamide groups (-C≡N) for NCN during the KSCN molten-salt treatment could be evidenced by the XPS (Figure S1), that NCN obtains the three characteristic N1s peaks at 398.4 eV, 399.3 eV and 400.8 eV assigned to triangular edge nitrogen, amino groups and central tertiary nitrogen [8], respectively, similar to the N1s XPS of GCN.

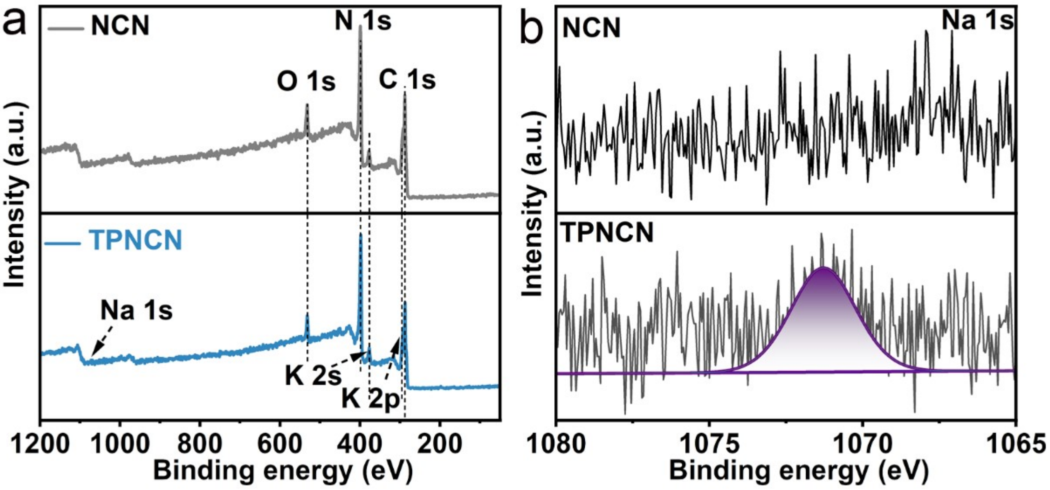

**Figure S2.** XPS spectra of NCN and TPNCN. a) survey spectrum, b) Na 1s.

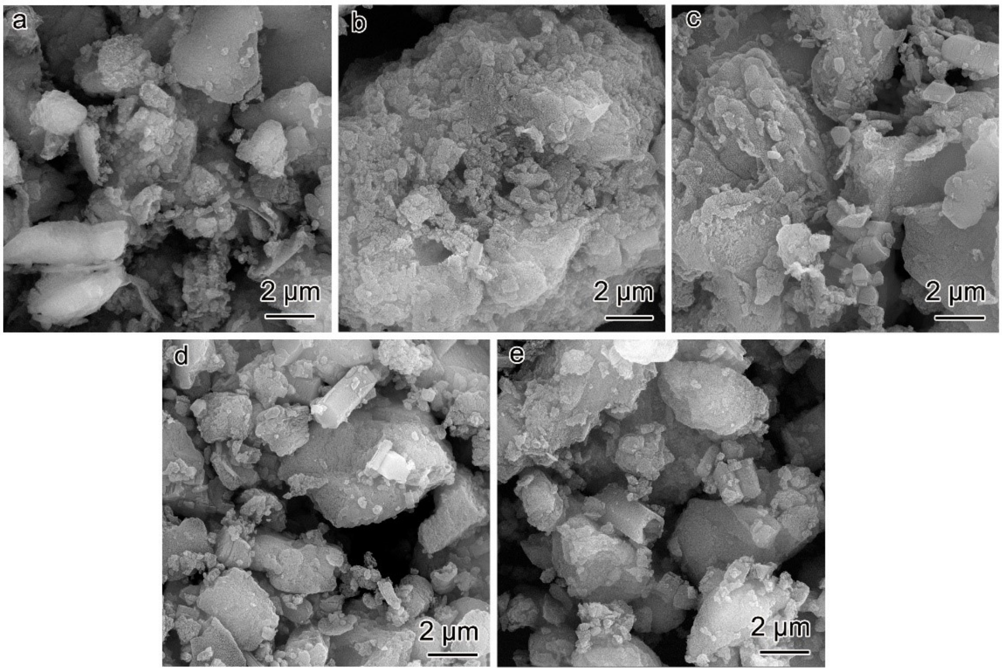

**Figure S3**. SEM of GCN, NCN, TPNCN1, TPNCN5 and TPNCN10.

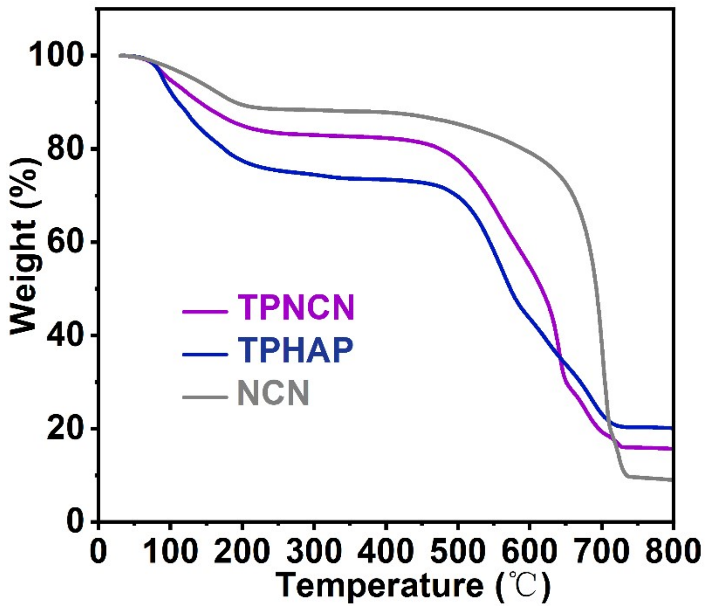

**Figure S4**. The thermogravimetry of TPHAP, NCN and TPNCN.

To investigate the thermal stability of samples, thermogravimetry analysis (TGA) was carried out in the air atmosphere. In the temperature range of 130-200 °C, TG curves of all the samples display a slight decrease, due to the $H_2O$ molecules adsorbed on the surface of samples [9]. Significantly, TPNCN and TPHAP exhibits high thermal stability below 500 °C and the NCN presents decomposition above 600 °C.

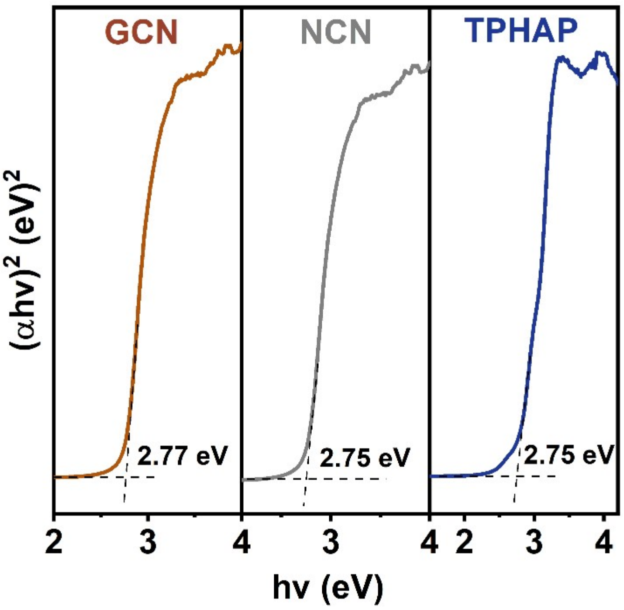

**Figure S5**. Tauc plots and bandgaps of GCN, NCN and TPHAP calculated from the Kubelka-Munk method.

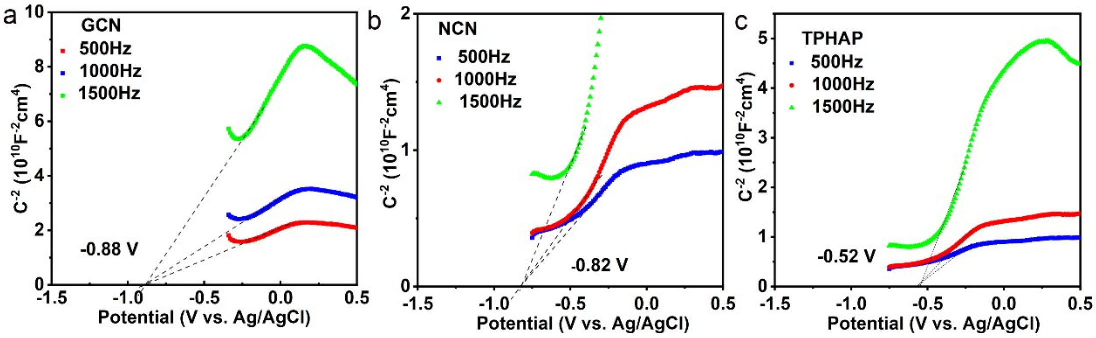

**Figure S6**. Mott-Schottky (M-S) plots of a) GCN, b) NCN and c) TPHAP.

As shown in **Figure S6**, the flat-band potentials of GCN, NCN and TPHAP are -0.88 V, -0.82 V and -0.52 V (vs. Ag/AgCl, at PH 7), respectively, which are also equal to -0.71 V, -0.65 V and -0.35 V (vs NHE, at PH 7), respectively.

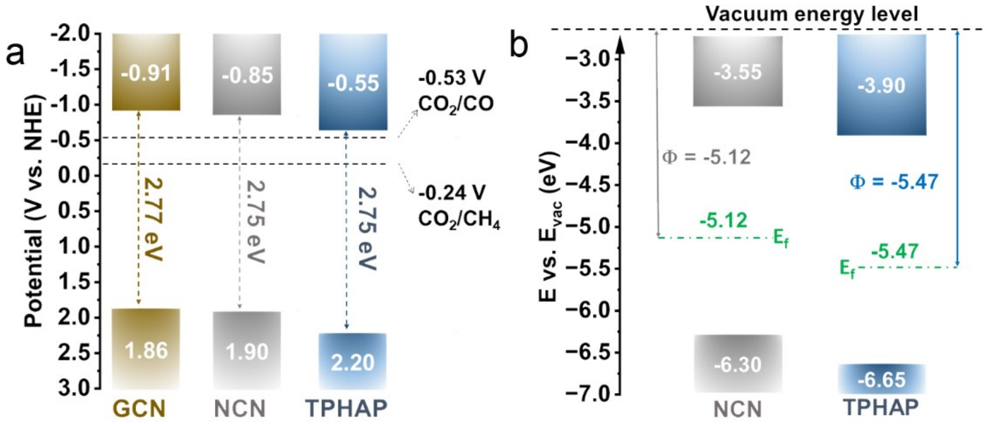

**Figure S7**. Schemed band structures of GCN, NCN and TPHAP calculated from a) the UV-visible diffuse reflectance spectra and Mott-Schottky (M-S) plots and b) the UV-visible diffuse reflectance spectra and Ultraviolet photoelectron spectroscopy (UPS).

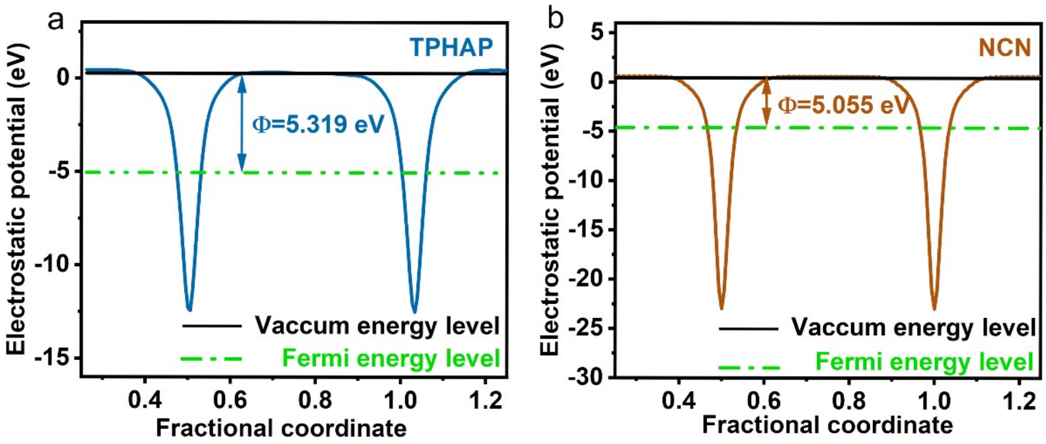

**Figure S8**. Electrostatic potentials for a) TPHAP and b) NCN.

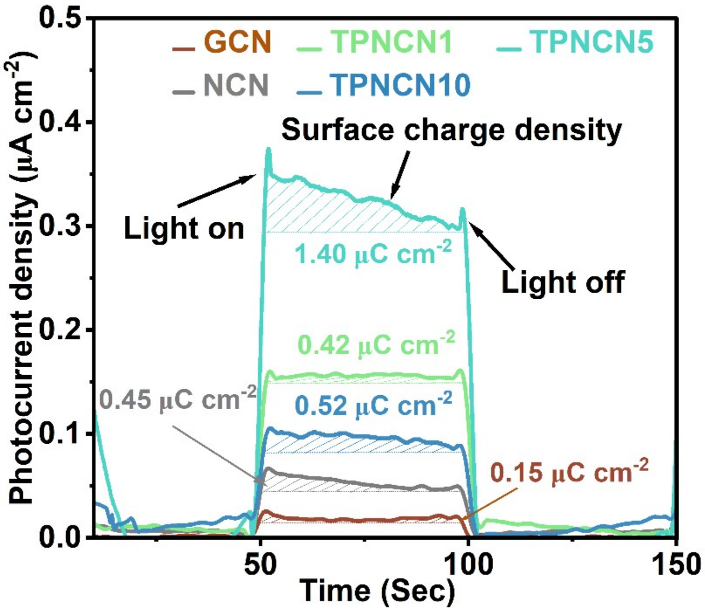

**Figure S9**. The surface charge density measured by transient photoelectric response.

The built-in electric field magnitude is calculated according to the Kanata' method [10-11] as following equation:

$$F_s = \sqrt{\frac{-2 \times V_s \times \rho}{\varepsilon \times \varepsilon_0}}$$

In this equation, the $F_s$, $V_s$, $\rho$, $\varepsilon$ *and* $\varepsilon 0$ is the built-in electric field, surface voltage, surface charge density, low-frequency dielectric constant and permittivity of free space, respectively.

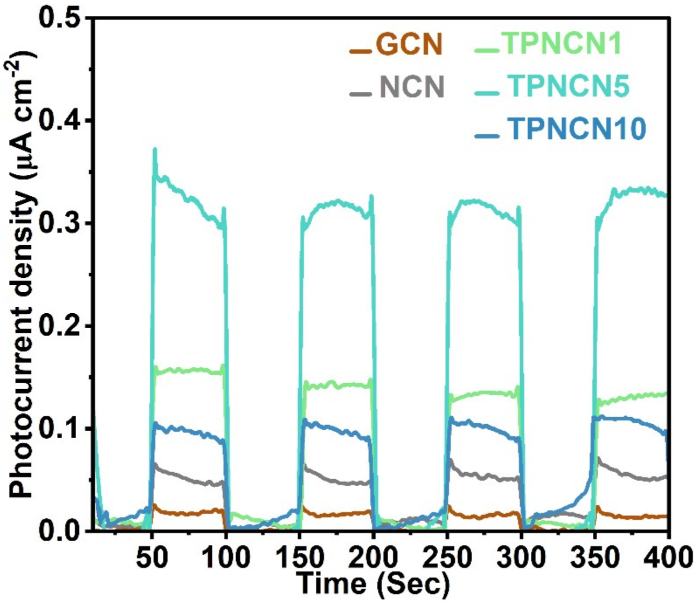

**Figure S10**. Photocurrent of GCN, NCN and TPNCN*m*.

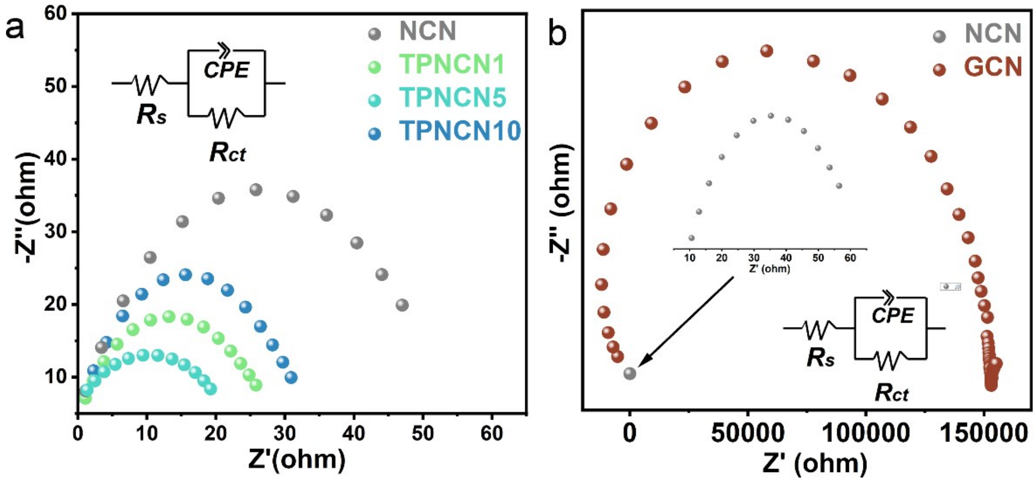

**Figure S11**. Electrochemical impedance of a) NCN and TPNCN*m* and b) GCN and NCN. Inset: $R_s$, *CPE*, and $R_{ct}$ are consistent of solution resistance, constant phase elements and charge transfer resistance through the electrode/electrolyte interface.

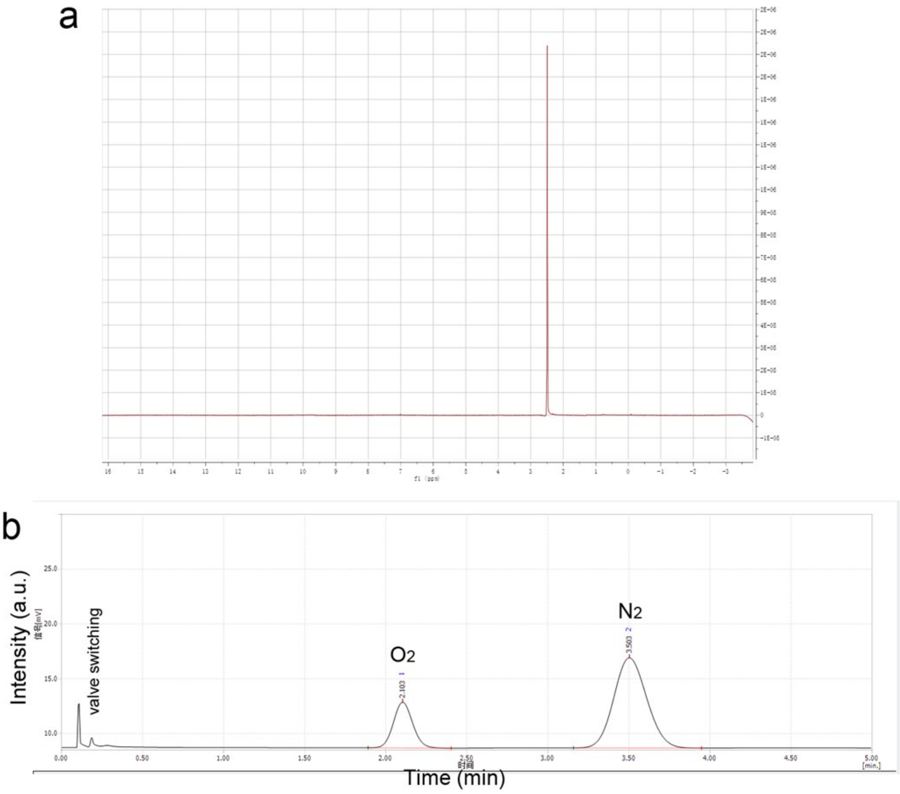

**Figure S12**. a) $^1$H-NMR spectrum of $CO_2$ photoreduction products in DMSO-$d_6$. b) The photocatalytic reaction products detected by gas chromatograph with a thermal conductivity detector(TCD).

To identify the liquid products after $CO_2$ photoreduction, the photocatalysts were gathered and dispersed in DMSO-$d_6$ under ultrasonication to dissolve the potential liquid products adsorbed on the surface of photocatalysts. Figure S12a demonstrates that no liquid products were detected through this procedure.

Additionally, in Figure S12b, the appearance of $H_2$ with retention at 1.09 min could be hardly detected after 8 h $CO_2$ photoreduction, indicating no $H_2$ production in this gas-solid $CO_2$ photoreduction reaction.

It is essential to note that the detection of products from the photocatalytic $CO_2$ reduction reaction was conducted in an off-line reactor. Consequently, the accuracy of $O_2$ detection was compromised due to interference from atmospheric $O_2$.

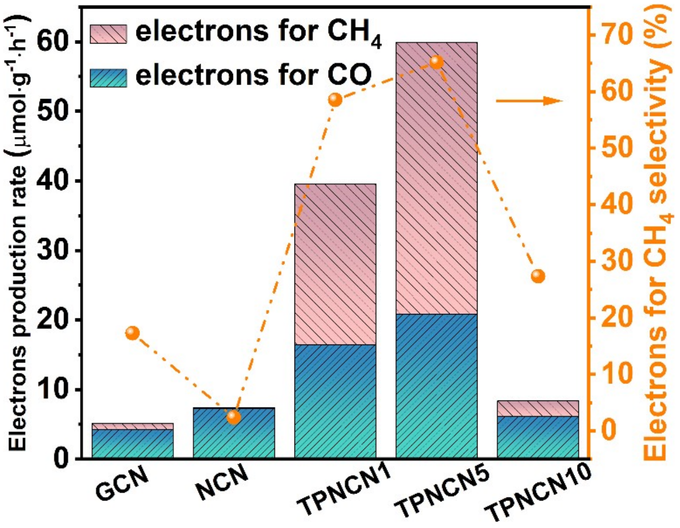

**Figure S13**. Evolution rates of electrons get involved in $CO_2$ photoreduction reaction and the electrons selectivity by generating $CH_4$.

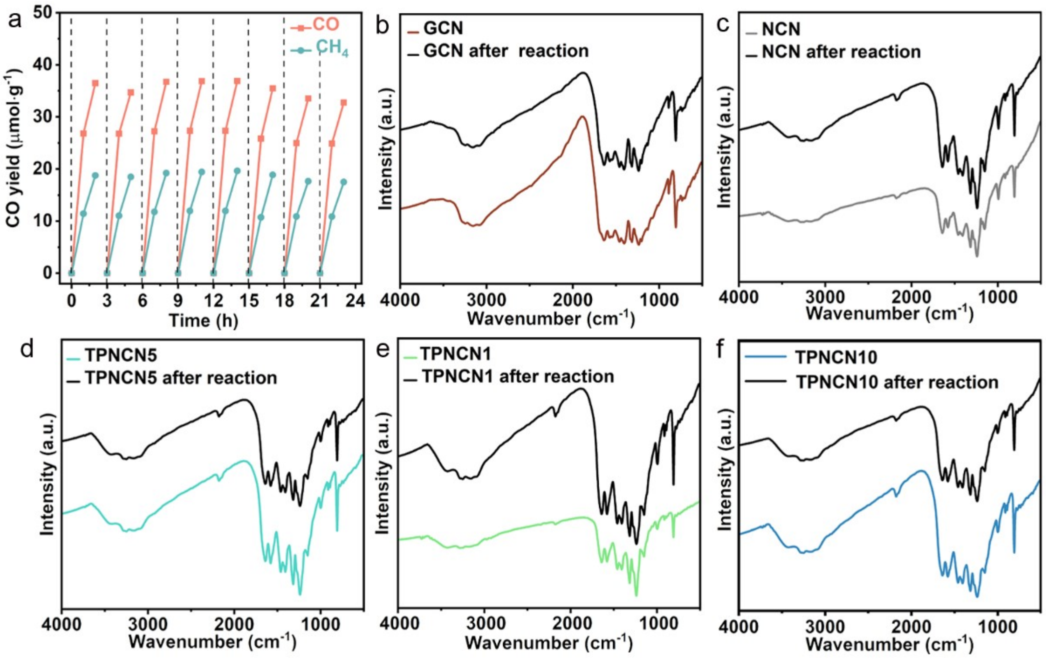

**Figure S14**. a) Time dependent CO and $CH_4$ production over TPNCN5. b-f) FTIR spectra of GCN, NCN, and TPNCN*m* before and after photocatalytic $CO_2$ reduction reaction.

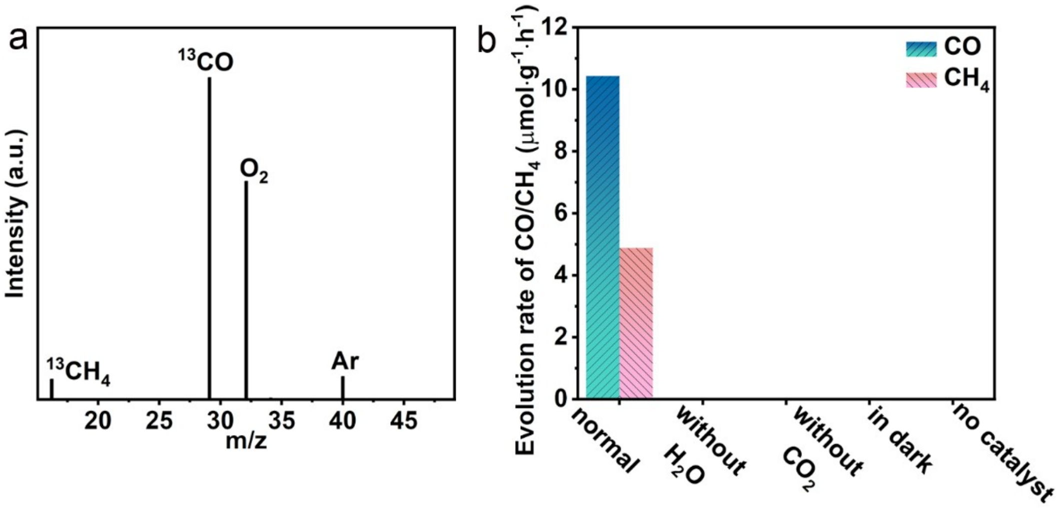

**Figure S15**. a) Mass spectra of $CO_2$ photoreduction products with $^{13}CO_2$ isotope as carbon source. b) Production rates of CO and $CH_4$ over TPNCN5 with control experiment.

To confirm the origin of CO and $CH_4$ produced from $CO_2$ reduction, the isotopic $^{13}CO_2$ was used as the carbon source in the $CO_2$ photoreduction reaction. As depicted in Figure S15a, the detection of $^{13}CO$ (m/z = 29) and $^{13}CH_4$ (m/z = 17) confirms that the products of CO and $CH_4$ indeed originate from $CO_2$.

To confirm the role of $H_2O$, light and photocatalyst for photocatalytic $CO_2$ performance, three different control experiments of without $H_2O$, in the dark and without photocatalyst were carried out. As illustrated in Figure S15b, products could be hardly detected after 8 h $CO_2$ photoreduction without $H_2O$, or in the dark, or no photocatalyst. This confirms that the photocatalytic $CO_2$ photoreduction is indeed driven in the presence of photocatalyst and $H_2O$ under irradiation.

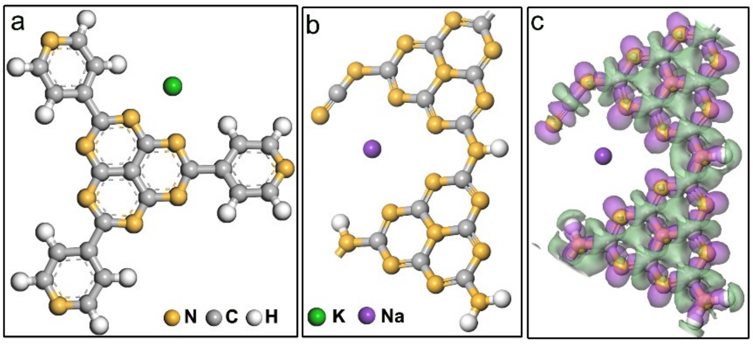

**Figure S16**. Optimized structural models of a) TPHAP and b) tri-s-triazine unit in NCN. Charge density difference of tri-s-triazine unit in NCN. Green and purple regions represent electron depletion and accumulation, respectively.

**Table S1**. Layer spacing and full width at half maximum (FWHM) were obtained from the (002), (100), (020), and (110) peaks in XRD patterns of GCN, NCN, and TPNCN*m*.

| | GCN | NCN | TPNCN1 | TPNCN5 | TPNCN10 |
|---|---|---|---|---|---|
| FWHM | 1.424 | 1.107 | 1.110 | 1.109 | 1.082 |
| $d_{002}$ (Å) | 3.249 | 3.163 | 3.163 | 3.163 | 3.163 |
| $d_{100}$ (Å) | 6.595 | / | / | / | / |
| $d_{020}$ (Å) | / | 8.525 | 8.674 | 8.537 | 8.631 |
| $d_{110}$ (Å) | / | 10.740 | 10.870 | 10.700 | 10.630 |

**Table S2**. Integral area percentages of N 1s peaks for GCN and NCN measured by XPS.

| peaks name | GCN (%) | NCN (%) |
|---|---|---|
| 398.4 (N1) | 18.0 | 20.7 |
| 399.3 (N2) | 23.8 | 20.3 |
| 400.8 (N3) | 58.2 | 59.0 |

N1, N2 and N3 are triangular edge nitrogen, amino groups and central tertiary nitrogen [12], respectively.

**Table S3**. Band gap, conduction band and valence band position of GCN, NCN and TPHAP calculated from UV-visible diffuse reflectance spectra and Mott-Schottky (M-S) plots.

| Samples | GCN | NCN | TPHAP |
|---|---|---|---|
| $E_g$ (eV) | 2.77 | 2.75 | 2.75 |
| $E_{VB}$ (V Vs. NHE) | 1.86 | 1.90 | 2.20 |
| $E_{CB}$ (V Vs. NHE) | -0.91 | -0.85 | -0.55 |

Eg, $E_{VB}$ and $E_{CB}$ are band gap values, valence band potential and conduction band potential, respectively.

**Table S4**. Work function, conduction band ($E_{CB}$) and valence band ($E_{VB}$) position of NCN and TPHAP calculated from UPS and UV-visible diffuse reflectance spectra.

| Samples | NCN | TPHAP |
|---|---|---|
| Work function (Φ Vs. VAC) | -5.12 eV | -5.47 eV |
| $E_{VB}$ (E Vs. VAC) | -3.55 eV | -3.90 eV |
| $E_{CB}$ (E Vs. VAC) | -6.30 eV | -6.65 eV |
| $E_{VB}$ (V Vs. NHE) | -0.95 V | -0.6 V |
| $E_{CB}$ (V Vs. NHE) | 1.80 V | 2.15 V |

**Table S5.** Photocatalytic $CO_2$ reduction performances of previously reported PCN-based photocatalysts.

| Catalysts | Light source | Reaction condition | CO production rate (μmol·g$^{-1}$·h$^{-1}$) | Ref |
|---|---|---|---|---|
| TPNCN5 | 300-W Xe lamp | gas-solid, water | 10.43 | This work |
| g-$C_3N_4$/$ZnIn_2S_4$ | 300-W Xe lamp | gas-solid, water | 12.5 | 13 |
| Cu/CN-0.25 | 300-W Xe lamp | gas-solid, $Na_2CO_3$+$H_2SO_4$ | 11.21 | 14 |
| HCONTP-200 | 300-W Xe lamp | gas-solid, $Na_2CO_3$+$H_2SO_4$ | 3.3 | 15 |
| K/S@CN-0.5 | 10-W Vlight lamp | gas-liquid-solid, KOH solution | 16.27 | 16 |
| Cu-CCN | 300-W Xe lamp | gas-solid, water | 3.136 | 17 |
| $Cs_3Bi_2Br_9$/g-$C_3N_4$ | 300W Xe lamp | gas-solid, water | 14.22 | 18 |
| $Fe_3N$/$Fe_2O_3$/g-$C_3N_4$ | 300W Xe lamp with 420 nm cut-off filter | gas-solid, water | 16.06 | 19 |
| BiCN-0.6 | 300W Xe lamp with AM 1.5G filter | gas-solid, water | 3.78 | 20 |

## References

[1] J. Liu, Y. Liu, N. Liu, Y. Han, X. Zhang, H. Huang, Y. Lifshitz, S. T. Lee, J. Zhong, Z. Kang, *Science*, 2015, **347**, 970.

[2] V. W. Lau, I. Moudrakovski, T. Botari, S. Weinberger, M. B. Mesch, V. Duppel, J. Senker, V. Blum, B. V. Lotsch, *Nat. Commun.*, 2016, **7**, 12165.

[3] Y. Yakiyama, A. Ueda, Y. Morita, M. Kawano, *Chem. Commum.*, 2012, **48**, 10651.

[4] L. Zhai, X. She, L. Zhuang, Y. Li, R. Ding, X. Guo, Y. Zhang, Y. Zhu, K. Xu, H. J. Fan, S. P. Lau, *Angew. Chem. Int. Ed.* 2022, **61**, e202116057.

[5] C. Cheng, B. He, J. Fan, B. Cheng, S. Cao, J. Yu, *Adv. Mater.* 2021, 2100317.

[6] S. J. Clark, M. D. Segall, C. J. Pickard, P. J. Hasnip, M. I. J. Probert, K. Refson, M. C. Payne, *Cryst. Mater.*, 2005, **220**, 567.

[7] G. Li, J. Han, H. Wang, X. Zhu, Q. Ge, *ACS Catal.,* 2015, **5**, 2009.

[8] Y. Li, Y. Wang, C. L. Dong, Y. C. Huang, J. Chen, Z. Zhang, F. Meng, Q. Zhang, Y. Huangfu, D. Zhao, L. Gu, S. Shen, *Chem. Sci.*, 2021, **12**, 3633.

[9] T. Chen, W. Zhang, B. Li, W. Huang, C. Lin, Y. Wu, S. Chen, H. Ma, *ACS Appl. Mater. Interfaces*, 2020, **12**, 56385.

[10] P. Lefebvre, J. Allègre, B. Gil, H. Mathieu, N. Grandjean, M. Leroux, J. Massies, P. Bigenwald, Phys. Rev. B, 1999, 59, 15363.

[11] G.Morello, F. Della Sala, L. Carbone, L. Manna, G. Maruccio, R. Cingolani, M. De Giorgi, Phys. Rev. B, 2008, 78, 195313.

[12] Y. Li, Y. Wang, C. L. Dong, Y. C. Huang, J. Chen, Z. Zhang, F. Meng, Q. Zhang, Y. Huangfu, D. Zhao, L. Gu, S. Shen. *Chem. Sci.*, 2021, **12**, 3633.

[13] F. Wang, S. Chen, J. Wu, W. Xiang, L. Duan, *Ind. Eng. Chem. Res.,* 2023, **62**, 15907.

[14] J. Wang, T. Heil, B. C. Zhu, C. W. Tung, J. G. Yu, H. M. Chen, M. Antonietti and S. W. Cao, *ACS Nano*, 2020, 14, 8584.

[15] R. Cheng, H. Jin, M. B. J. Roeffaers, J. Hofkens, E. Debroye, *ACS Omega*, 2020, **5**, 38, 24495.

[16] Z. Liu, J. Ma, M. Hong, R. Sun, *ACS Catal.*, 2023, **13**, 2106.

[17] Y. Li, B. Li, D. Zhang, L. Cheng, Q. Xiang, *ACS Nano*, 2020, **14**, 10552.

[18] Y. Baghdadi, F. Temerov, J. Cui, M. Daboczi, E. Rattner, M. S. Sena, I. Itskou, S. Eslava, *Chem. Mater.,* 2023, **35**, 8607.

[19] C. Wang, B. Rhimi, M. Radervand, *J. Alloy. Compd.,* 2021, **852**, 156955.

[20] J. Gu, R. Guo, Y. Miao, Y. Liu, C. Wu, C. Duan, W. Pan, *Energy Fuels*, 2021, **35**, 10102.